How Biorecognition Affects the Electronic Properties of Reduced Graphene Oxide in Electrolyte-Gated Transistor Immunosensors

Matteo Sensi, Rafael Furlan de Oliveira, Marcello Berto, Alessandro Paradisi, Pierpaolo Greco, Carlo Augusto Bortolotti, Paolo Samorì, Fabio Biscarini

ADVANCED FUNCTIONAL MATERIALS
www.afm-journal.de

How Biorecognition Affects the Electronic Properties of Reduced Graphene Oxide in Electrolyte-Gated Transistor Immunosensors

*Matteo Sensi, Rafael Furlan de Oliveira, Marcello Berto, Alessandro Paradisi, Pierpaolo Greco, Carlo Augusto Bortolotti, Paolo Samorì, and Fabio Biscarini**

Ambipolar electrolyte-gated transistors (EGTs) based on reduced graphene oxide (rGO) have been demonstrated as ultra-sensitive and highly specific immunosensors. However, the physics and chemistry ruling the device operation are still not fully unraveled. In this work, the aim is to elucidate the nature of the observed sensitivity of the device. Toward this aim, a physical–chemical model that, coupled with the experimental characterization of the rGO-EGT, allows one to quantitatively correlate the biorecognition events at the gate electrode and the electronic properties of rGO-EGT is proposed. The equilibrium of biorecognition occurring at the gate electrode is shown to determine the apparent charge neutrality point (CNP) of the rGO channel. The multiparametric analysis of the experimental transfer characteristics of rGO-EGT reveals that the recognition events modulate the CNP voltage, the excess carrier density Δn, and the quantum capacitance of rGO. This analysis also explains why hole and electron carrier mobilities, interfacial capacitance, the curvature of the transfer curve, and the transconductances are insensitive to the target concentration. The understanding of the mechanisms underlying the transistor transduction of the biorecognition events is key for the interpretation of the response of the rGO-EGT immunosensors and to guide the design of novel and more sensitive devices.

1. Introduction

During the last decade, gate-functionalized electrolyte-gated transistors (EGTs) emerged as ultrasensitive biosensors.[1–7] However, an in-depth quantitative analysis of its results is still missing. In most cases, the dose curve, built out of the electronic response in the current of the transistor, mainly from the transfer curves recorded at different analyte concentrations, is fit to an isotherm, such a Langmuir type, Hill type,[8] or other less common isotherms, e.g., Frumkin,[9] Guggenheim–Anderson–Bethe,[10] uniform Langmuir type.[11,12] This practice rests on three underlying assumptions: a) the system is at chemical equilibrium, b) the concentration (more precisely the activity) of the specific probe is notably inferior when compared to one of the target analytes, and c) the signal of the transducer (measured as relative variation of an observable with respect to a control experiment) is linearly correlated with the population of occupied sites of the probe used for specific recognition. These three assumptions often do not hold in relevant experimental scenarios, for instance, the one in a) upon non-equilibrium conditions or in flow experiments (*vide sub*), the one in b) when the concentration of analyte is ultra-low, while for c) it may be true in the linear region of the transistor, but not in others. If on the one hand, this bias may not affect the shape of the dose curve, it poses serious limits both on the correctness of conclusions about the biorecognition events,

M. Sensi, M. Berto, A. Paradisi, C. A. Bortolotti, F. Biscarini
Department of Life Sciences
Università degli Studi di Modena e Reggio Emilia
via Campi 103, Modena 41125, Italy
E-mail: fabio.biscarini@unimore.it

The ORCID identification number(s) for the author(s) of this article can be found under https://doi.org/10.1002/adfm.202313871

DOI: 10.1002/adfm.202313871

R. F. de Oliveira, P. Samorì
CNRS
ISIS
Université de Strasbourg
8 allée Gaspard Monge, Strasbourg 67000, France

R. F. de Oliveira
Brazilian Nanotechnology National Laboratory (LNNano) CNPEM
Campinas 13083-970, Brazil

P. Greco
Department of Neuroscience and Rehabilitation
Università degli Studi di Ferrara
via Luigi Borsari, 46, Ferrara 44121, Italy

P. Greco, F. Biscarini
Center for Translational Neurophysiology of Speech and Communication – Istituto Italiano di Tecnologia
Via Fossato di Mortara 17–19, Ferrara 44121, Italy

and, also on the extraction of quantitative parameters related to the sensing experiment, such as the limit of detection , the association constants, or other thermodynamic parameters that require a more insightful level of analysis that should encompass the operational gate voltages (V_{GS}).

More importantly, the transistor current transfer curve that gives origin to the dose curve, and ultimately to the sensor parameters, depends on the type of material used, such as organic polymers, organic molecules, carbon nanotubes, graphene, and related materials, or others. One can reasonably argue that the transfer curve significantly differs depending on the materials used and the relevant interfaces. Their devices would exhibit different subthreshold regions and linear and saturation regimes, and in the case of materials that exhibit ambipolar behavior, there might be no significant off-current. A qualitative attempt to correlate the sensitivity to the exponential density of states of an ordered organic semiconductor was reported for pentacene.[13] No universal approaches aimed to model the transduction of the biorecognition event in terms of the properties of the transistor active material in the description of the sensor were made.

This paper aims to answer the central, yet unaddressed, question for EGT immunosensors: what is the relation between the biorecognition events and the response of the device in terms of the electronic properties of the active material used in the transistor channel? Responding to this query not only will bring important knowledge into the field, but also enable researchers to establish a rational method of analysis that treats the whole set of experimental data, without loss of information or discretional selection of data, for instance, the arbitrary delimitation of the linear regime, or the a priori assumption on the type of isotherm. Electrolyte-gated transistor biosensors can also operate in time-dependent experiments,[14–16] or upon administration of pulsed voltage trains,[17] or upon a flux in microfluidics circuits,[13,18] where the dose curves are extracted from the time-dependent response. These time-dependent experiments, which are also based on some initial assumptions on the kinetics of biorecognition, will not be discussed in this paper, as the present work is conceived to describe systems under thermodynamic equilibrium.

The contribution of our approach stems from the semiconductor constitutive equations of the electronic structure of reduced graphene oxide (rGO) and the thermodynamics equations of equilibrium, which allows us to avoid phenomenological assumptions and treat the specific biorecognition on the same footing as the electronic structure of the channel material. The main results consist of the identification of the effect of biorecognition on some of the relevant materials properties, and, not intuitively, the explanation of the concentration-independence of both the curvature at the charge neutrality point (CNP) and the transconductance.

In Section 2, we describe the equilibrium established at the gate electrode first upon incubation in the target analyte solution, and then when immersed in the gating electrolyte of the EGT. The gate electrode is functionalized with an antibody as the probe. In Section 3, we analyze how the resulting equilibrium affects the electro-chemical potential profile of the rGO-EGT and derive the expression for the voltage at the charge neutrality point versus concentration of the target analyte that allows us to extract both the true equilibrium constant of binding between antibody and target, and the density of antibodies which is an important process parameter. In Section 4, we determine the capacitances and analytically solve the equation describing the free energy profile in the rGO-EGT for the excess charge carrier density in the rGO channel. Finally, we derive an analytical expression for the ambipolar transfer curve of rGO-EGT immunosensors that contains the information on the biorecognition events, and from there we extract the values of charge carrier mobilities and capacitances.

2. Equilibrium of the Gate Electrode with the Electrolyte

2.1. Equilibrium Between Gate Electrode and Target Analyte Solution

In our model, we first describe the ex-situ incubation of the gate electrode, functionalized with the recognition probe, in an aqueous solution containing the target analyte, by expressing the binding constant of the probe/analyte pair. In this way, we determine how the equilibrium occupation of the probe molecules bound to the gate electrode is determined by the analyte concentration. This part of the model can be applied also to any functionalized electrode and is not characteristic of rGO transistors.

Figure 1a schematically shows the functionalized gate incubated in the target analyte solution of initial concentration $[X]_0 = c$ and then exposed to the electrolyte bridging gate and channel in the rGO-EGT. In Figure 1a, the electrode is incubated in a solution containing a target analyte, and the binding process at the gate (G) surface can be written as: $X_{(sol)} + P_{(G)} \rightleftarrows PX_{(G)}$.

The surface binding is assumed to obey thermodynamic equilibrium governed by the association constant K_a:

$$K_a = \frac{[PX]_G}{[P]_G\,[X]} = exp\left(-\frac{\mu_{0PX} - \mu_{0P} - \mu_{0X}}{RT}\right) \quad (1)$$

where [X] is the concentration of the free analyte in solution, $[P]_G$ of the free probe on the gate electrode, and $[PX]_G$ of the probe bound to the target analyte on the gate electrode at equilibrium. In the sensor literature, it is often reported the dissociation constant $K_d = 1/K_a$. The μ_0 terms are the standard chemical potentials of the different species, while R is the ideal gas constant and T is the temperature in kelvin. Consistently with equilibrium equations, all concentrations should be considered as activities, expressed in molarity values without the physical dimension M (mol dm^{-3}) for solutions else as molar density in mol dm^{-2} for adsorbed species.

Based on the control experiments,[19] we neglect the non-specific adsorption. Then, the initial analyte concentration $c = [X] + [PX]_G$ and the initial probe concentration on the gate electrode $[P]_{G0} = [P]_G + [PX]_G$ both express mass conservation. Then, we re-write Equation (1) as $[PX]_G = K_a\,([P]_{G0} - [PX]_G)(c - [PX]_G)$, whose physical solution yields the gate bound fraction $[PX]_G/[P]_{G0}$ as:

$$\frac{[PX]_G}{[P]_{G0}} = \frac{\{1 + K_a c + K_a[P]_{G0}\} - \sqrt{1 + 2K_a\,(c + [P]_{G0}) + K_a^2\,(c - [P]_{G0})^2}}{2K_a[P]_{G0}} \quad (2)$$

Equation (2) expresses the equilibrium fraction of the probe-target bound to the gate, at a given concentration c, as a function

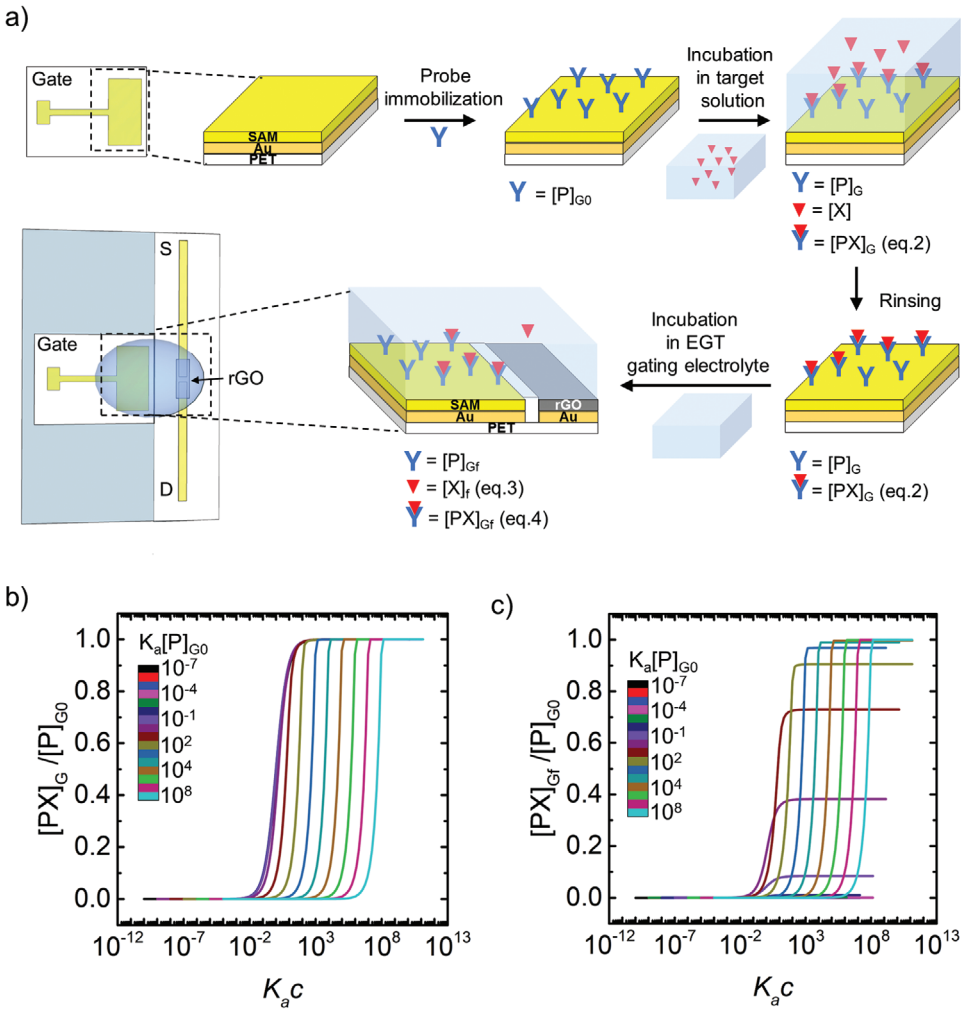

Figure 1. Equilibria involving the gate electrode. a) Scheme of the equilibrium established upon incubation of the gate electrode in the solution containing the target and of the equilibrium established upon dissolution of the bound target into the gating electrolyte of the rGO. The figure schematically depicts the probes (antibodies) in light blue, the red inverted triangles representing the target analyte. b) Plot of the equilibrium bound pair fraction $[PX]_G/[PX]_{G0}$ versus $K_a c$ for different $K_a[P]_{G0}$, from 10^{-7} (black) to 10^8 (pale blue) for the incubation in target solution. c) Equilibrium fraction $[PX]_{Gf}/[P]_{G0}$ versus $K_a c$ for different values of $K_a[P]_{G0}$ from 10^{-7} (black) to 10^8 (pale blue), for the incubation in EGT gating electrolyte.

of the initial probe concentration $[P]_{G0}$ on the gate electrode and the equilibrium constant K_a. Here, $[P]_{G0}$ depends on the functionalization process of the gate electrode, and thus can be used to assess the reproducibility of the functionalization protocol. For small c values ($c<<1/K_a$ which means on the left tail of the dose curve) the Taylor series expansion of Equation (2) yields $\frac{[PX]_G}{[P]_{G0}} \approx \frac{K_a c}{1+K_a[P]_{G0}}$. This is consistent with the linear increase of the target bound fraction at low c values. The slope is ca equal to K_a for $K_a[P]_{G0}<<1$; smaller than K_a when $K_a[P]_{G0} \leq 1$ (implying that not all probe is bound), while it tends to $1/[P]_{G0}$ when $K_a[P]_{G0}>>1$ when the probe is bound. This outcome hints at the fact that the sensing gate endowed with a high probe concentration (compared to $1/K_a$ value) will capture all analyte molecules in the solution. We highlight that for $K_a[P]_{G0}>>1$ the fraction of bound analyte $[PX]_G/[P]_{G0} \approx \frac{c}{[P]_{G0}}$ is independent of the K_a value, with the apparent constant of the linear response being proportional to $1/[P]_{G0}$. Since in literature it is common to associate the fraction $[PX]_G/[P]_{G0}$ to the immunosensor signal, and the slope of the linear response to the equilibrium constant K_a, this result demonstrates that this assumption may be wrong in some conditions as high affinity constant/high probe density.

Figure 1b shows the concentration-dependence of the target-bound fraction of the probe for the equilibrium with the target-containing solution. We discuss the curves in view of the renormalized variable $K_a c$ for different values of $K_a[P]_{G0}$. For $K_a[P]_{G0} \leq 1$ the curves collapse into a curve resembling Langmuir isotherm, viz. they are all linear versus $K_a c$ around $K_a c = 1$ with their linear trend spanning $\approx \pm 2$ decades around the inflection point. All curves saturate to the unity plateau for $K_a c>>K_a[P]_{G0}$. The slope is steeper when K_a $[P]_{G0}>1$ with the slope equal to $1/[P]_{G0}$ as explained in the previous paragraph. The curves exhibit a horizontal shift to the right for increasing $K_a[P]_{G0}$ (whose value is the inflection point). To summarize, Langmuir-type trend is

when $K_a[P]_{G0} \leq 1$, viz. low probe concentration and/or low K_a, while the trend is superlinear for $K_a[P]_{G0} > 1$. The curves that obey the condition $K_a[P]_{G0} < 1$, collapse around the same inflection point (weakly dependent on K_a). We infer from these simple equilibrium considerations that the deviations from the "true" Langmuir-type behavior shall be expected when $K_a[P]_{G0} > 1$, which is consistent with a functionalization process yielding high probe density and/or large equilibrium constant. The process-dependent parameter $[P]_{G0}$ determines the apparent binding constant of a (pseudo)Langmuir isotherm that in the literature is often fitted through the experimental data. This is a *caveat* about the heuristic, acritical, adoption of Langmuir (or other isotherms) in interpreting the data from the immunosensor and extracting from them a value for the affinity binding constant.

We point out that this equilibrium model directly applies to the case of EGT immunosensors where the electrolyte containing the target analyte is also used to operate the EGT immunosensor. The only strong condition of our model is that the non-specific adsorption of the analyte is neglected both onto the electrode (here the gate, which is however functionalized with an anti-fouling bovine serum albumin(BSA)/self-assembled monolayer(SAM) bilayer in the voids) and onto the semiconductor channel of the EGT device.

2.2. Equilibrium Between Incubated Gate Electrode and Gating Electrolyte

After the incubation, the gate electrode is immersed in the PBS electrolyte that connects the gate electrode to the rGO channel, as depicted in the second row of Figure 1a. Once the EGT is contacted through an electrolyte not containing the analyte, a new equilibrium is established in the rGO-EGT and a fraction of the analyte can be released from the probe, attaining its final equilibrium concentration $[X]_f = \frac{[PX]_G - [X]_f}{\{[P]_{G0} - [PX]_G + [X]_f\}K_a}$. We solve for $[X]_f$ to obtain:

$$[X]_f = \frac{-\{1 - K_a[PX]_G + K_a[P]_{G0}\} + \sqrt{\{1 - K_a[PX]_G + K_a[P]_{G0}\}^2 + 4K_a[PX]_G}}{2K_a} \quad (3)$$

By plugging Equation (2) in Equation (3), we obtain the fraction of the probe bound to the analyte on the gate after the final equilibrium is attained in the rGO-EGT:

$$\frac{[PX]_{Gf}}{[P]_{G0}} = \frac{1}{2K_a[P]_{G0}} \left\{ \left\{ 2 + K_a\left(c - [PX]_G\right) + 2K_a[P]_{G0} \right\} - \sqrt{1 + 2K_a\left(c + [P]_{G0}\right) + K_a^2\left(c - [P]_{G0}\right)^2} - \sqrt{\{1 - K_a[PX]_G + K_a[P]_{G0}\}^2 + 4K_a[PX]_G} \right\} \quad (4)$$

As expected, the equation returns 0 when $c = 0$. In analogy with Figure 1b, in Figure 1c we plot the equilibrium values of $[PX]_{Gf}/[P]_{G0}$ (the free analyte $[X]_f/[P]_{G0}$ will be its complement to unity) as a function of $K_a c$ for various values of $K_a[P]_{G0}$. When $K_a [P]_{G0} < 1$ the fraction of electrode-bound analyte $[PX]_{Gf}/[P]_{G0}$ is very small and becomes almost negligible in the regime where $K_a[P]_{G0} << 1$. The analyte initially bound to the functionalized electrode is, de facto, completely detached at any concentration c, thus the electrode is insensitive to the analyte concentration. This appears as close-to-zero-value darker lines. Hence, to avoid the consequent loss of sensitivity toward most of the bound analyte from the gate electrode, it is necessary that the electrode attains a probe concentration of at least $[P]_{G0} \approx < 1/K_a$. This condition is indeed obeyed by the medium-light curves in Figure 1c, from $K_a[P]_{G0} = 0.01$ to $K_a[P]_{G0} = 1$. When $K_a [P]_{G0} >> 1$ the fraction of bound analyte $[PX]_{G0}/[P]_{G0}$ is dominant with respect to the fraction $[X]_f/[P]_{G0}$ in solution. This is indeed the condition recommended for effective sensing aimed to minimize the casual non-specific adsorption on non-functionalized device interfaces.

In brief, this simple analytical calculation provides us a guideline for the design rule of the sensor, completely general from the nature of the target analyte. Finally, we point out that all the curves in Figure 1c exhibit that the range where the electrode is mostly sensitive to the concentration c is the region that stretched about two decades around the inflection point. Thus, the range of maximum sensitivity is set by the thermodynamic affinity binding constant as well as by the initial probe concentration of the gate electrode. This highlights, once more, the importance of the electrode functionalization step in maximizing the performance of the immunosensor.

The equilibrium equations, upon the assumptions made, are independent of the channel material, thus they may apply to any EGT immunosensor (and possibly EGT sensors with aptamers, oligopeptides, and oligonucleotides establishing a one-to-one association with the target analyte) whereby biorecognition takes place exclusively on the gate.

3. Electrostatics of the rGO-EGT

3.1. Voltage Profile Across the rGO-EGT

Now we calculate the potential profile across the whole rGO-EGT, to obtain the voltage difference $V_{GS} - V_{CNP}$ between the applied gate voltage V_{GS} with respect to the charge neutrality point V_{CNP} which is the minimum of the transfer curve where an equal concentration of charge carriers (holes and electrons) in rGO exists. Then, we relate it to the excess charge carrier density in rGO.

We start the model from literature, e.g., Refs. [20–24] that describes the capacitive coupling in the rGO-EGT, and we modify it by explicitly introducing the voltage drop at all relevant interfaces that exist in the rGO-EGT immunosensor.[25,26] These are depicted in **Figure 2a**. Starting from the rGO-electrolyte interface, the electrolyte bath potential $V_b(c)$ is shifted by the final equilibrium concentration of the analyte $[X]_f$ as $V_b(c) = V_{b,0} + \frac{\mu_{0,Xb}}{qF} + \frac{RT}{qF} \ln [X]_f(c)$. Here F is the Faraday constant, and q is a nominal charge that accounts for electrostatic effects associated to the species involved in the equilibrium. The potential $V_{b,0}$ relates to the chemical potential of the electrolyte in the absence of the target analyte.

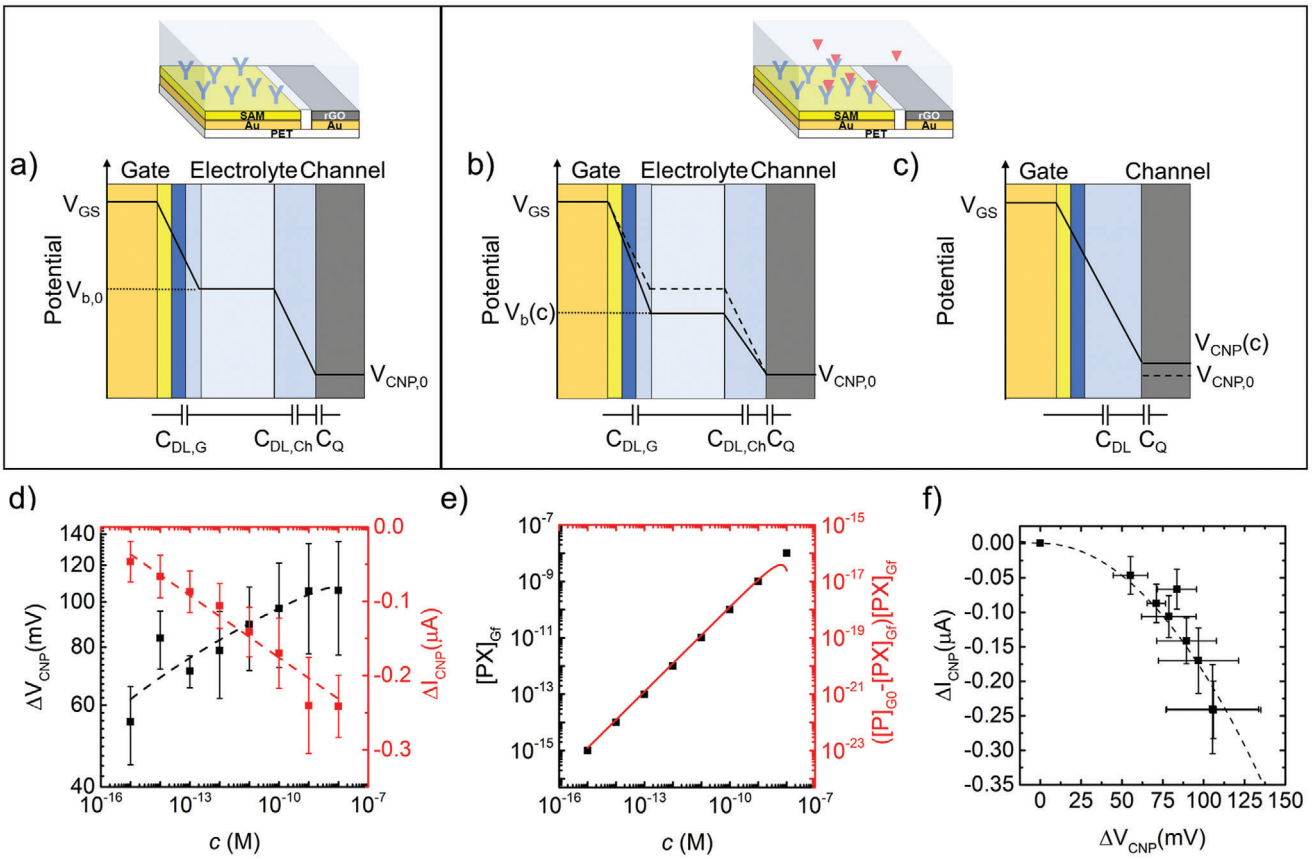

Figure 2. Electrostatic potential profile across the EGT a) without and b) with the target analyte bound to the probe on the gate electrode. The colors of the layers reflect the ones in the upper sketches. c) Electrostatic potential profile as described by Equation (8). d) Fit of the ΔV_{CNP} versus c experimental values using Equation (10). Each data point (filled square) is the mean value obtained from 5 datasets, with the standard error of the mean as error bars. The weighted best fit line (dashed line) is shown and the best fit parameters values are $K_a = 1.81 \times 10^{11}$, $[P]_{G0} = 1.24 \times 10^{-8}$, $q = 8.44$, $\mu_{0,PXG}+\mu_{0,PG} = 181$ kJ mol^{-1}. In red the mean ΔI_{CNP} versus c is shown, with a dashed line linear fit to guide the eye. e) The black squares are the values of $[PX]_{Gf}$ versus c calculated with Equation (4) and introducing the parameters K_a and $[P]_{G0}$ determined from the fit in panel (d). The red line is the conditional probability $([P]_{G0}-[PX]_{Gf})[PX]_{Gf}$ versus c. f) Fit of the mean ΔI_{CNP} versus ΔV_{CNP}. The dashed line is the result of the best fit of Equation (16). The error bars are the standard error of the mean (SEM) obtained from five datasets.

The voltage drop between the electrolyte bath and rGO is distributed between two terms on the right-hand side of the next equation:[26]

$$|V_b(c) - V_{CNP,0}| = e|\Delta n|\left(\frac{1}{C_q(\Delta n)} + \frac{1}{C_{DL,Ch}}\right) = \frac{\hbar|v_{F,rGO}|\sqrt{\pi|\Delta n|}}{e} + \frac{|\Delta n|\cdot e}{C_{DL,Ch}} \quad (5)$$

The first contribution is ascribed to the quantum areal capacitance[20,27–31] of rGO:

$$C_q(\Delta n) = \alpha\frac{e^2\sqrt{|\Delta n|}}{\hbar|v_F|\sqrt{\pi}} = \frac{e^2\sqrt{|\Delta n|}}{\hbar|v_{F,rGO}|\sqrt{\pi}} \quad (6)$$

Here, rGO is treated as a pure 2D graphene rescaled by a factor α that accounts for the chemical inhomogeneity of rGO and the appearance of the band gap in place of the Dirac point; the second term in Equation (5) is ascribed to the areal capacitance $C_{DL,Ch}$ of the electrical double layer due to ion re-organization at the interface with the rGO channel. The two in-series areal capacitances C_q and $C_{DL,Ch}$ are schematically depicted in Figure 2a–c. The term to the left of Equation (5) expresses the potential difference gating the rGO channel, whose potential is pinned by the potential source, as shown in Figure 2b. The change of the potential difference at the rGO/electrolyte interface induces the variation of the charge carrier areal density Δn in the rGO channel, as described by the right-hand side of Equation (5). The charge neutrality voltage $V_{CNP,0}$ is referred to as the rGO in the electrolyte bath in the absence of the analyte; $\hbar$ is the reduced Planck constant. We term as $v_{F,rGO}$ the Fermi velocity v_F of Dirac electrons in graphene[22,32] divided by the disorder parameter α. We assume that both C_q and $C_{DL,Ch}$ have the same electroactive area, which is appropriate for rGO in an electrolyte medium, but not in the solid state. This implies that the rGO layers sum up their respective single-layer quantum capacitances as they were in parallel (and not in series despite the stacked architecture) and the interfacial surface accessible to ions scales as the

number of layers or nominal thickness. In other words, this assumption underlines a "volumetric scaling" of the capacitance of rGO, a feature that is considered distinctive of OECTs rather than EGTs.

The gate voltage drop depends on the equilibria on the gate $[PX]_{Gf}$. Because the gate electrode is connected to the high-force channel of an SMU, also its potential is held constant. Then the changes in gate functionalization will shift the bath electrochemical potential by the same amount but with a negative sign. We depict the voltage profile with the rapid drop at each interface with the electrolyte in the right column of Figure 2b. The shift of the electrolyte bath potential changes the potential drop at the gate-electrolyte interface. The charge generated in the rGO channel will be:

$$\left|V_{GS} - V_b(c) - \frac{\mu_{0,PXG}}{qF} - \frac{\mu_{0,PG}}{qF} - \frac{RT}{qF} ln\left\{[PX]_{Gf}(c)\,[P]_{Gf}(c)\right\}\right|$$

$$A_G C_{DL,G} = e\,|\Delta n|\,A_{Ch}\left(N_l + 1\right) \quad (7)$$

which allows us to express the electrolyte bath potential as:

$$V_b(c) = V_{GS} - \frac{e\,|\Delta n|\,A_{Ch}\left(N_l + 1\right)}{A_G C_{DL,G}} - \left\{\frac{\mu_{0,PXG}}{qF} + \frac{\mu_{0,PG}}{qF} + \frac{RT}{qF} ln\left([PX]_{Gf}(c)\,[P]_{Gf}(c)\right)\right\} \quad (8)$$

Here, we introduce the geometrical area of the gate A_G and the areal electrical double-layer capacitance on the gate electrode $C_{DL,G}$. The effective (electroactive) rGO channel area equals $A_{ch}(N_l + 1)$, with A_{ch} being the geometric channel area and N_l the number of active rGO layers. The number $N_l + 1$ encompasses the whole ion-accessible surface area of the electrolyte solution. By plugging Equation (8) into Equation (6), the equation governing the dependence of Δn from c becomes:

$$\left|V_{GS} - V_{CNP}(c)\right| = \frac{\hbar\,|v_{F,rGO}|\,\sqrt{\pi\,|\Delta n|}}{e} + \frac{e\,|\Delta n|}{C_{DL}(c)} \quad (9)$$

where $V_{CNP}(c)$ is the concentration-dependent voltage of the charge neutrality point expressed as:

$$V_{CNP}(c) = V_{CNP,0} + \frac{RT}{qF} ln\left\{\left([P]_{G0} - [PX]_{Gf}\right)[PX]_{Gf}\right\} + \left(\frac{\mu_{0,PXG}}{qF} + \frac{\mu_{0,PG}}{qF}\right) \quad (10)$$

Figure 2c shows the shift $\Delta V_{CNP}(c) = V_{CNP}(c) - V_{CNP,0}$ from Equation (10) by the contribution to the electrochemical potential of the anchored probe and probe target. The dependence on the concentration c is embodied in $[PX]_{Gf}(c)$ from Equation (4). We notice that the capacitance $C_{DL}(c)$ is absent in Equation (10).

3.2. How to Extract K_a from the Shift of the Charge Neutrality Point

We start now to use our analysis on the experimental data that were reported recently[19] with the rGO-EGT immunosensor for anti-drug (Infliximab) antibody. The gate is functionalized with the antibody anti-TNFα Infliximab grafted within the architecture already described. The drawing in Figure 2a helps us later to understand the modeling of the interfacial gate capacitance.

The first operation that we carry out is the fit of the shift ΔV_{CNP} versus c in Equation (10) using four variational parameters (K_a, $[P]_{G0}$, q and $\mu_{0G} = \mu_{0,PXG} + \mu_{0,PG}$) and upon fixing and releasing one parameter in the fitting process. This procedure yields the equilibrium association constant K_a and the initial probe activity on the gate electrode $[P]_{G0}$.

The results of the fitting procedure with Equation (10) are shown in Figure 2d. The best fit yields $K_a \approx 10^{11}$ and $[P]_{G0} \approx 10^{-8}$ M. This value agrees with the reported K_a of Infliximab-ATI used here ($\approx 10^{10}$–10^{11}).[33] This finding confirms the importance of choosing a probe with a large value of the affinity binding constant K_a for a robust response of the biosensor at low x concentrations.

Figure 2e shows the resulting concentration-dependent fraction of the bound probe as from Equation (2). Hence, the large K_a value makes the electrode in the rGO-EGT retain a comparable composition as in the equilibrium with the target-containing solution, an ideal situation where the measurement conditions do not strongly perturb the initial electrode composition. We point out that in this range of ultralow concentrations, where $[P]_{G0} >> c$, the operations occur in a regime that is distant from the one described by the Langmuir equilibrium that holds for $[P]_{G0} << c$. Since the shift of the CNP potential depends on (the logarithm of) the product $[P]_{Gf}[PX]_{Gf}$, we readily recognize the origin of both the straight line (following the trend of $[PX]_{Gf}$ at concentration $c << [P]_{G0}$) and the slow decreasing trend of $[P]_{Gf}$ at concentration $c \approx [P]_{G0}$. Their (logarithm of the) product, whose meaning is a conditional probability to find a probe binding site available at a certain concentration, is correlated with the observed rGO shift of the CNP. The amount of charge exchanged during the recognition q takes a best fit value of the order of 8. Whether this corresponds to an actual charge exchanged in the recognition event, as in a faradic process, we cannot be certain, so we suggest caution in this interpretation. However, it may underlie a substantial electrostatic energy reorganization during binding.

3.3. Interfacial Capacitance of the rGO-EGT

To solve Equation (9) for $\Delta n(c)$, we must then assign a concentration dependence to the in-series effective interfacial capacitance $C_{DL}(c)$ that is derived as:

$$C_{DL}(c) = \left\{\frac{1}{C_{DL,Ch}} + \frac{A_{Ch}\left(N_l + 1\right)}{A_G}\frac{1}{C_{DL,G}(c)}\right\}^{-1} \quad (11)$$

The interfacial channel capacitance $C_{DL,Ch}$ and N_l are determined from the experimental data of the current as fitting parameters, as it will be detailed in Section 4. In the following, we explain how to calculate $C_{DL,G}$. The gate electrode, which was already sketched in Figure 2 of Ref., [19] is functionalized by three different layered species: the SAM (mixed self-assembled monolayer of mercaptoundecanoic acid and mercapto-hexanol 1:3), the free probes (Infliximab, IFX) and the probes bond to the analyte (infliximab and antibodies toward Infliximab, IFX+ATI).

Table 1. Estimated values of the different components of the gate areal capacitance in Equation (12). The values for C_{SAM}, C_P, and C_{PX} are calculated from the dielectric constant of the specific layer on the gate (ϵ_{layer}) and the thickness of the capacitor (d). The values for $C_{SAM,P}$, and $C_{SAM,PX}$ are estimated as for in-series capacitors. The vacuum permittivity is $\epsilon_0 = 8.85\times10^{-12}$ F m^{-1}.

Areal Capacitance	Equation	ϵ_{layer}	Molecular height d [nm]	Estimated values of Areal Capacitance [F m^{-2}]
C_{SAM}	$\approx \frac{\epsilon_{SAM}\epsilon_0}{d_{SAM}}$	2.1[35]	1.5[35]	1.2×10^{-2}
C_P	$\approx \frac{\epsilon_P\epsilon_0}{d_P}$	20[36]	11	1.6×10^{-2}
C_{PX}	$\approx \frac{\epsilon_{PX}\epsilon_0}{d_{PX}}$	20	22	8.1×10^{-3}
$C_{SAM,P}$	$\approx (\frac{1}{C_{SAM}}+\frac{1}{C_P})^{-1}$	NA	$\approx$ 12.5	7.0×10^{-3}
$C_{SAM,PX}$	$\approx (\frac{1}{C_{SAM}}+\frac{1}{C_{PX}})^{-1}$	NA	$\approx$ 34.5	4.9×10^{-3}

Because the covering layer is not homogenous, we model $C_{DL,G}$ as three in-parallel capacitors:

$$C_{DL,G}(c) = C_{SAM}\theta_{SAM} + C_{SAM,P}(1-\theta_{SAM})\left(1-\frac{[PX]_{Gf}(c)}{[P]_{G0}}\right) + C_{SAM,PX}(1-\theta_{SAM})\left(\frac{[PX]_{Gf}(c)}{[P]_{G0}}\right) \quad (12)$$

where the SAM contributes the areal capacitance C_{SAM}, the free probe C_P, and the probe bound to the analyte C_{PX}. We assume here that $C_{DL,G}$ does not depend on V_{GS}, which implies that we neglect the contribution due to the polarization of the electrode. To avoid over-parametrization, we look at structural models of the relevant molecules in the literature to fix the molecular thicknesses and dielectric constants of SAM and probe layers and calculate the capacitance values as detailed in **Table 1** with their references. The coverage θ_{SAM} is the fraction of the gate electrode area covered by the SAM, hence depends only on the gate functionalization with the probe through the parameter $[P]_{G0}$. We estimate θ_{SAM} by multiplying the surface-projected area of the probe molecule A_{probe} by the areal density of the probe $\frac{[P]_{G0}\cdot V\cdot N_A}{A_G}$:

$$\begin{cases}\theta_{SAM}([P]_{GO}) = 1-\frac{A_{probe}\cdot[P]_{GO}\cdot V\cdot N_A}{A_G} & \text{for } \theta_{SAM}\geq 0\\ \theta_{SAM}([P]_{GO}) = 0 & \text{otherwise}\end{cases} \quad (13)$$

where A_{probe} is estimated in our work equal to 68 nm^2 from model structures of the antibody IFX[34] assuming a standing antibody with the *fc* arm perpendicular to the surface, V is the volume of the drop of solution that contains the target analyte where the rGO-EGT is immersed (50 μl in this experiment) and N_A is the Avogadro constant. Notice that here $[P]_{G0}$ has its physical dimensions (M), differently from the previous equations. The formulation of the coverage in Equation (13) as a stepwise function avoids unphysical negative results for high $[P]_{G0}$.

The second and third contributions in Equation (12) represent the areal fractions of free probe and bound probe respectively, that depend also on the concentration c of the target analyte through $[PX]_{Gf}(c)$ Equation (4). Using the values reported in Table 1 and the value $\theta_{SAM} = 0.79$ (which implies that the recognition antibody covers only 21% of the gate surface) estimated from Equation (13), we are now able to calculate the gate areal capacitance $C_{DL,G}(c)$ without any further fitting procedure from Equation (12) at each c value. The corresponding curve is shown in **Figure 3a** (blue bold line). This curve undergoes a variation of less than 5% across the concentration range explored.

As a comparison, the trends expected for other $[P]_{G0}$ values (and the corresponding coverages) are shown as thinner lines, for two limit values of the affinity binding constant K_a. We notice that at the lowest concentrations, the capacitance is nearly constant to a plateau, and does not exhibit a dependence on the value of K_a. For "small" $K_a = 10^5$ (dashed lines) the gate capacitance is insensitive to the analyte concentration. Instead for "large" $K_a = 10^{11}$ (continuous lines) the gate capacitance exhibits a smooth monotonic decrease at concentrations $c < [P]_{G0}$, and a more rapid variation when c is around $[P]_{G0}$. The rapid variation is enhanced for larger $[P]_{G0}$ hence smaller coverage θ_{SAM}. For $c > [P]_{G0}$ the trend saturates to a plateau either equal to (in the case of low K_a) or lower than (in the case of high K_a) of the one at the low concentrations. The monotonic decrease is more evident for small θ_{SAM}, meaning a larger coverage by the probe.

The effective interfacial capacitance C_{DL}versus concentration is displayed in Figure 4b for various values of $C_{DL,Ch}$. It shows a very smooth variation of fractions of a few percent across the concentration range, depending on the value of $C_{DL,Ch}$ and N_l. This suggests that the interfacial capacitance does not play a major role here in the sensing mechanism of the rGO-EGT immunosensor. The concentration dependence of the quantum capacitance C_q versus c and the total capacitance of the rGO-EGT $C_{tot} = \{\frac{1}{C_q(c)}+\frac{1}{C_{DL}(c)}\}^{-1}$ will be discussed in Section 5.3.

4. Charge Carrier Density and Current in rGO-EGT

We now address the response of the rGO-EGT and the observables from the electrical characterization of rGO-EGT. In Section 4.1, we solve analytically Equation (9) to show the dependence of the concentration on the charge carrier density shift $\Delta n(c)$. Then, in Section 4.2, we derive the analytical expression for the rGO-EGT current that allows us to global fit the transfer curves in Section 5.1, from which we obtain the values of $C_{DL,c}$, the charge carrier mobilities of holes and electrons, the transconductances, and the dependence of the carriers at CNP on the concentration.

4.1. Concentration Dependence of the Charge Carrier Density

We now solve analytically Equation (9) by recasting it as: $V_{GS} - V_{CNP}(c) = f\frac{\hbar|v_{F,rGO}|\sqrt{\pi|\Delta n|}}{e} + \frac{\Delta n\cdot e}{C_{DL}(c)}$. The gate voltage difference $V_{GS}-V_{CNP}$(c) leads to the excess areal charge density $\Delta n = n_e - n_h$ between the charge carrier areal densities of electrons n_e and holes n_h. The sign of Δn is determined by the sign function $f = sgn(V_{GS} - V_{CNP}(c))$: for holes $V_{GS}-V_{CNP} \leq 0$ and $\Delta n \leq 0$; for electrons $V_{GS}-V_{CNP} \geq 0$ and $\Delta n \geq 0$. The two carrier densities are equal at the CNP: when $V_{GS}-V_{CNP} = 0$, $\Delta n = 0$.

The excess charge carrier areal density $\Delta n_0(c)$ at $V_{GS} = 0$ V is due not only to the doping/oxidation level of rGO, embodied in $V_{CNP,0}$, but also to the concentration of the target analyte and the functionalization of the gate electrode. When $c = 0$, Δn_0 arises

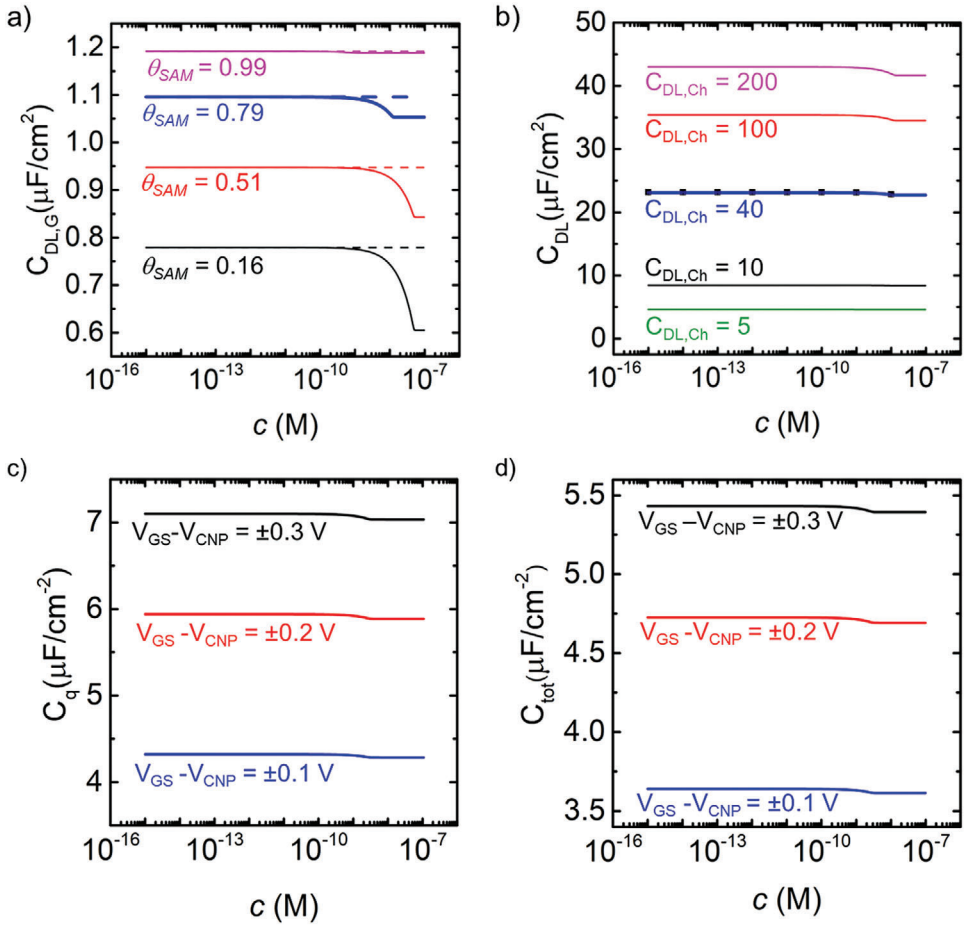

Figure 3. a) Gate capacitance $C_{DL,G}$ values, calculated with Equation (15), for different θ_{SAM}, obtained with different values of $[P]_{G0}$: 1×10^{-9} (magenta), 1×10^{-8} (blue, bold), 3×10^{-8} (red), 5×10^{-8} (black). In each plot, the solid lines were obtained with $K_a = 10^{11}$, while the dashed lines with $K_a = 10^5$. The blue bold line represents the $C_{DL,G}$ versus c curve calculated with the experimental values of K_a and $[P]_{G0}$ that we obtained from the fit in Figure 2d. b) Effective interfacial capacitance $C_{DL}(c)$ versus c plot at different $C_{DL,Ch}$ values: 5, 10, 40, 100, and 200 μF cm^{-2}. We take here $N_l = 1$ and $\theta = 0.79$. The blue bold line represents the $C_{DL}(c)$ versus c curve calculated with the experimental values of K_a and $[P]_{G0}$ that we determined from the fit in Figure 2d. The black dots are the C_{DL} values calculated from the transfer curve fitting in Section 5.3. c) C_q and d) C_{tot} versus c at different values of V_{GS}-V_{CNP}: ±0.1 V (blue), ±0.2 V(red), and ±0.3 V(black).

from the partial oxidation of rGO and should be regarded as due to excess/defect of electrons in partially (de)localized states that are formed due to the presence of oxidated carbon groups. It corresponds to the solution of $-V_{CNP,0} = f\frac{\hbar|v_{F,rGO}|\sqrt{\pi\Delta n_0}}{e} + \frac{\Delta n_0 \cdot e}{C_{DL}(0)}$. This implies that also the CNP of the rGO-EGT in the absence of the target analyte is not an exclusive rGO material property, as it also depends on the gate functionalization through the interfacial capacitance $C_{DL}(0)$ with the electrolyte.

At CNP of each concentration $V_{GS} = V_{CNP}$(c), where $\Delta n = 0$, the minimum current I_{CNP} is transported by n_{CNP} electrons and holes. For $V_{GS} = 0$ V and $V_{CNP} < 0$ V, the states in the gap of the Dirac (pseudo-)cones of rGO are populated with an excess of electrons and the electrochemical potential shift is positive with respect to CNP; for $V_{GS} = 0$ V and $V_{CNP} > 0$ V, electrons are removed from the gap and the electrochemical potential shift is negative. To summarize, the densities of the two charge carriers are obtained for $\Delta n > 0$ as $n_e = n_{CNP} + \Delta n$ and $n_h = n_{CNP}$; for $\Delta n < 0$ as $n_e = n_{CNP}$ *and* $n_h = n_{CNP} - \Delta n$.

Equation (9) is a second-order equation whose physically relevant solution is the root with a negative sign:

$$\Delta n = f \cdot n_0 \left[1 - \sqrt{1 + f\frac{C_{DL}\left(V_{GS} - V_{CNP}\right)}{e \cdot n_0}}\right]^2 \tag{14}$$

where we define the density of carriers $n_0 = \left(\frac{C_{DL}(c)\hbar|v_{F,rGO}|\sqrt{\pi}}{2e^2}\right)^2$. Equation (14) is symmetric around CNP. At the CNP, it yields $\Delta n = 0$, while in the proximity of the CNP where $\frac{C_{DL}|V_{GS}-V_{CNP}|}{e \cdot n0} \ll 1$, it exhibits a parabolic behavior $|\Delta n| \approx \frac{[C_{DL}(c)(V_{GS}-V_{CNP}(c))]^2}{4e^2 \cdot n0(c)} = \frac{e^2}{\hbar^2|v_{FrGO}|^2\pi}(V_{GS} - V_{CNP}(c))^2$. Equation (14) also yields the areal density of carriers $\Delta n_0(c)$ at $V_{GS} = 0$ which is the outcome of interfacial doping of the rGO channel once rGO is immersed in the electrolyte.

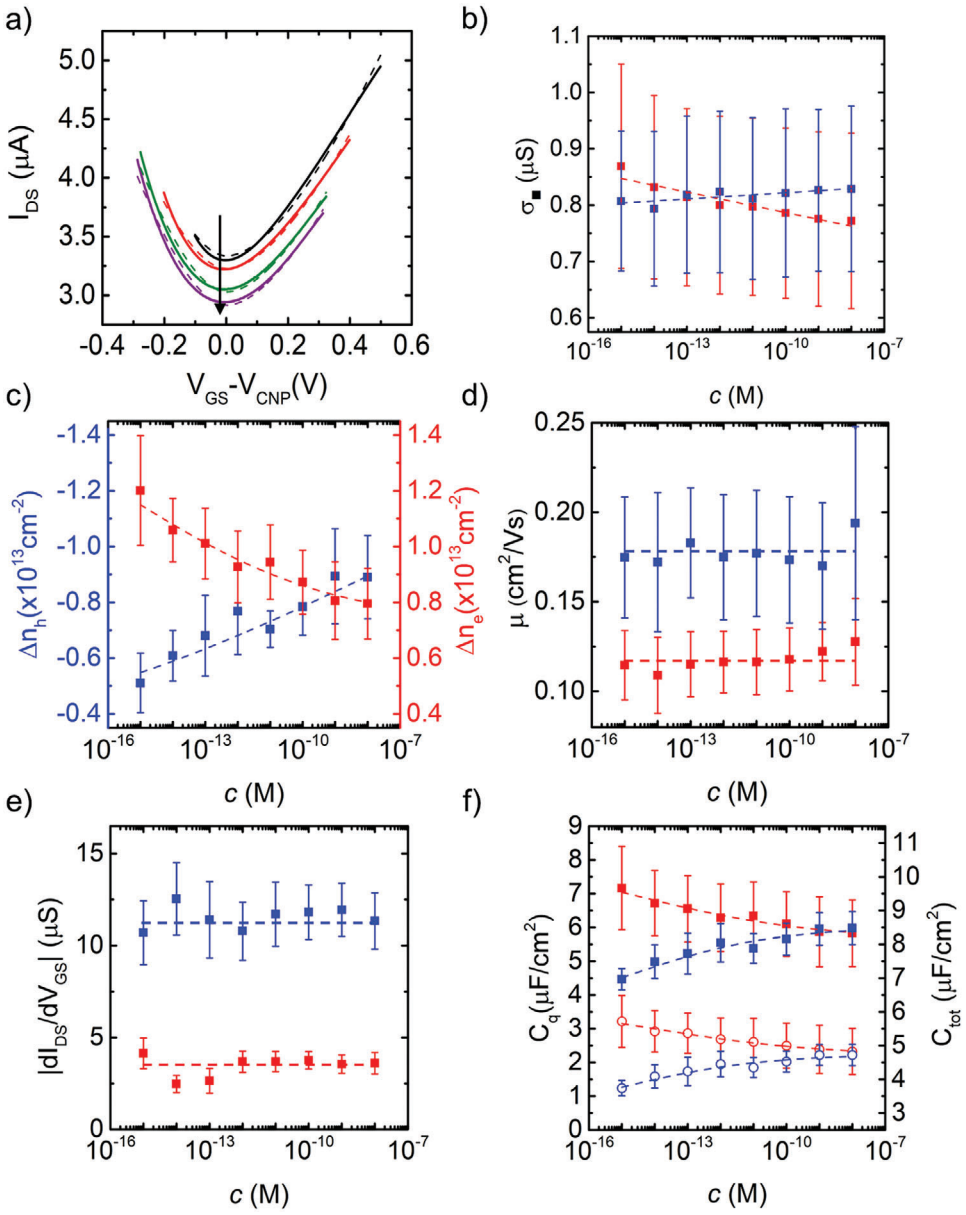

Figure 4. Fitting of rGO-EGT transfer curves. a) Examples of transfer curves with the device exposed to 0 M (solid black), 1 fM (solid red), 1 pM (solid green), and 1 nM (solid purple) target analyte. The dashed lines are the result of the best fit with Equation (15). Hole (blue) and electron (red) b) sheet conductance $\sigma_{\blacksquare}$ and c) excess charge density Δn versus c, extracted at $V_{GS} = -0.3$ and 0.3 V, respectively. d) hole (blue) and electron (red) charge carrier mobilities. Dashed lines are the mean values. e) Transconductance versus c at $V_{GS} = -0.3$ V (blue) and 0.3 V (red). Dashed lines are the mean values. f) (left) quantum capacitance Cq versus c with blue squares for holes and red for electrons; (right) the corresponding trend of the total capacitances C_{tot} versus c (empty circles).

We point out two important consequences of the result from Equation (14). Near the CNP the capacitance $C_{DL}(c)$ exactly cancels out with that in $n_0(c)$ thus the charge carrier density in the proximity of the minimum depends exclusively on $V_{CNP}(c)$. This supports the recently published evidence of the concentration-independent curvature of the current versus V_{GS}-$V_{CNP}(c)$ near the CNP that will be discussed in Section 5.1. Far from CNP, where $\frac{C_{DL}|V_{GS}-V_{CNP}|}{e n0} >> 1$ Equation (14) becomes $|\Delta n| \approx \frac{C_{DL}(c)|V_{GS}-V_{CNP}(c)|}{e}$ which describes the linear response of the rGO-EGT as the consequence of the dominant contribution of the interfacial capacitance in Equation (9). In this regime, the rGO-EGT responds as either an n-type or p-type transistor, depending on the sign of $V_{GS} - V_{CNP}(c)$.

4.2. Analytical Expression for the rGO-EGT Source–Drain Current

From the excess current density as from Equation (14), the current can be analytically expressed starting from linear response theory, by multiplying the areal density of charge carriers $\Delta n(c)$ by

the charge e, the mobility $\mu_{h(e)}$ for holes (electrons), the longitudinal electric field $\frac{V_{DS}}{L}$, L being the channel length, the channel width W. The whole transfer curve is described by the following formula:

$$I_{DS} = I_{CNP}(c) + \frac{W}{L} e n_0(c) \frac{\left[\mu_h \cdot (1-f) + \mu_e \cdot (1+f)\right]}{2} \left[1 - \sqrt{1 + \frac{C_{DL}(c)\left|V_{GS} - V_{CNP}(c)\right|}{e n_0(c)}}\right]^2 V_{DS} \quad (15)$$

where $I_{CNP}(c)$ is the minimum current at CNP contributed by an equal density of holes and electrons, and the function f determines the nature of the carriers transporting the excess current. Equation (15) states that, despite the symmetry of the excess charge carrier density in Equation (14) with respect to the CNP, the excess current is asymmetric because of the different mobilities of electrons and holes.

In the proximity of the CNP, the current in Equation (15) yields $I_{DS} \approx I_{CNP}(c) + \frac{W}{L}\frac{e^3}{2\pi\hbar^2} V_{DS} \frac{[\mu_h\cdot(1-f)+\mu_e\cdot(1+f)]}{|v_{F,rGO}|^2}[V_{GS} - V_{CNP}(c)]^2$ whose curvature $\frac{W}{L}\frac{e^3}{\pi\hbar^2} V_{DS} \frac{[\mu_h\cdot(1-f)+\mu_e\cdot(1+f)]}{|v_{F,rGO}|^2}$ is independent of the concentration of the target analyte, in agreement with the experimental observation in Ref. [19] This approximation explains how the curvature is a property of rGO through the charge carrier mobilities and the Fermi velocity, because of the parabolic behavior of the excess charge carrier density near the CNP. However, this model does not explain the dependence of I_{DS} on the area of the gate electrode that was also reported in Ref.[19]

5. Analysis of the rGO-EGT Ambipolar Transfer Characteristics

5.1. Global Fitting of the Transfer Curves of the rGO-EGT

The fitting of the excess current transfer curves at each analyte concentration is performed with Equation (15). The free parameters left in the fitting procedure are the charge carrier mobilities, μ_e and μ_h, the capacitance of the rGO channel $C_{DL,Ch}$, the number of layers N_l, and the Fermi velocity $v_{F,rGO}$. All other parameters were fixed by the procedure applied as in Figure 2d. In C_{DL} given by Equation (), the gate capacitance C_{DLG} is calculated with Equation (12) (this process-dependent property may vary depending on the characteristics of the gate electrode, e.g., polarizable versus non-polarizable, and area). The constants are $A_C = 2.4 \times 10^{-7}$ m^2, $A_G = 1.23 \times 10^{-5}$ m^2, the elementary charge e, W/L = 100, the reduced Planck constant $\hbar$, drain-source voltage $V_{DS} = 0.05$ V.

Figure 4a shows the result of the best fit with Equation 15 (dashed lines) of all transfer curves on one of the datasets, viz. same gate electrode and same channel and different concentration. The fit accurately reproduces (Adjusted $R^2 = 0.992$) the whole set of transfer curves throughout the operational voltage applied. Hence, Equation (15) describes the main observable of our rGO-EGT characterization, with no a priori criteria on the selection of data, as instead is customary in the analysis of OFET transfer curves within a priori identified regimes. The fit of the current converges rapidly with $N_l = 1$ (albeit the nominal thickness of the thin film is larger) which suggests that the active layer is dominated by the first one in contact with the electrodes.

In Figure 4b, we show the sheet conductance $\sigma_{\blacksquare} = (\frac{L}{W}\frac{I_{DS}}{V_{DS}})$ versus c. We notice that the hole sheet conductance (blue markers) is slightly increasing at $V_{GS} = -0.3$ V, while the electron conductance of the rGO-EGT at $V_{GS} = 0.3$ V is decreasing with a faster slope on the logarithmic scale.

In Figure 4c, we show the trends of the rGO-EGT excess charge carrier densities of electrons and holes as from Equation (14). The values of Δn, extracted at $V_{GS} = -0.3$ V and $V_{GS} = 0.3$ V, show a clear power law dependency versus the analyte concentration. The n-type charge carrier density (for $V_{GS} = 0.3$ V) decreases with increasing concentration, while the p-type charge carrier density (for $V_{GS} = -0.3$ V) increases (in absolute value) with increasing concentration. It is noticeable that the change of the charge carrier density (that leads to the excess current and the other relevant observables) is on the order of 50% of the initial value for the whole concentration range which spans seven orders of magnitude.

In Figure 4d, the values of the charge carrier mobilities (left axis) are concentration-independent, with the holes moving faster than electrons. We estimate their mean value to be $\mu_e = 0.118 \pm 0.019$ cm^2 V^{-1} s^{-1} and $\mu_h = 0.179 \pm 0.037$ cm^2 V^{-1} s^{-1}, close to mobility values found for rGO thin films.[22,37,38] The Fermi velocity $v_{F,rGO}$ is insensitive to the concentration, its value is $8.29 \pm 0.37 \times 10^5$ m s^{-1}, smaller than the value 1×10^6 m s^{-1} reported for graphene. This yields the disorder[39,40] parameter $\alpha \approx 1.2$.

We now comment on the role and the interplay of interfacial and quantum capacitances. The best fit value of the electrolyte/rGO capacitance for the whole data set as in Figure 4a is $C_{DL,Ch} \approx 40\ \mu$Fcm^{-2}, which yields the interfacial capacitance $C_{DL}(c)$ depicted in Figure 3b. Its values reveal that the interfacial capacitance is modestly sensitive to concentration. Together with the finding of the concentration-independent charge carrier mobilities, this result confirms that their product, which is proportional to the rGO transconductance of holes and electrons, will be modestly dependent on concentration, as previously observed.[19] The transconductance values are shown in Figure 4e.

After ruling out charge carrier mobilities and interfacial capacitance as the properties imparting sensitivity, it emerges clearly that the "culprit" for sensitivity is the quantum capacitance $C_q(c)$, which exhibits a rapid variation versus c as shown in Figure 4f. The quantum capacitance, being in series with the interfacial capacitance $C_{DL}(c)$, being smaller dominates the total capacitance $C_{tot}(c)$ of the rGO-EGT also shown in Figure 4f. This result has a particular relevance as it demonstrates that it is a channel material property that endows the device with the amplification of the specific biorecognition, and consequently, with the sensitivity.

5.2. The Minimum Current I_{CNP} Versus V_{CNP}

Once we fit the excess current, obtaining the set of best fit parameters discussed in Section 5.1, we relate the properties at the CNP. The minimum current $I_{CNP}(c) = \frac{W}{L} e(n_{CNP} + \Delta n_0(c))[\mu_h + \mu_e] V_{DS}$ is transported by an equal density of holes and electrons $n_{CNP} + \Delta n_0(c)$, where the areal density

of dopants n_{CNP} is dictated only by the chemical nature of the rGO upon its reduction process and does not depend on the electrolyte. The excess $\Delta n_0(c)$ is inferred from Equation (14) with $V_{GS} = 0$. Owing to the variability among devices, it is more robust to recast this relation in terms of the shift of the minimum current at $\Delta I_{CNP}(c)$:

$$\Delta I_{CNP}(c) = \frac{W}{L} e \left\{ f\left(V_{CNP}\right) \cdot n_0(c) \left[1 - \sqrt{1 + \frac{C_{DL}(c) \left| V_{CNP}(c) \right|}{e \cdot n_0(c)}} \right]^2 \right\} \left[\mu_h + \mu_e\right] V_{DS} - \frac{W}{L} e \left\{ f\left(V_{CNP}\right) \cdot n_0(0) \left[1 - \sqrt{1 + \frac{C_{DL}(0) \left| V_{CNP}(c) \right|}{e \cdot n_0(0)}} \right]^2 \right\} \left[\mu_h + \mu_e\right] V_{DS} \quad (16)$$

whose approximation for $\frac{C_{DL}|V_{CNP}|}{e \cdot n_0} \ll 1$ as a function of the shift $\Delta V_{CNP}(c)$ reads $\Delta I_{CNP}(c) \approx \frac{W}{L} \frac{8e^3 \langle \mu \rangle V_{DS}}{\hbar^2 |v_{F,rGO}|^2 \pi} \{ f(V_{CNP}) V_{CNP}^2(c) - f(V_{CNP,0}) V_{CNP,0}^2(c) \}$. This is expanded as:

$$\Delta I_{CNP}(c) \approx f\left(V_{CNP}\right) \frac{W}{L} \frac{8e^3 \langle \mu \rangle V_{DS}}{\hbar^2 \left| v_{F,rGO} \right|^2 \pi} \left\{ \Delta V_{CNP}^2(c) + 2 V_{CNP,0} \Delta V_{CNP}(c) + \left[1 - \frac{f\left(V_{CNP,0}\right)}{f\left(V_{CNP}(c)\right)} \right] V_{CNP,0}^2 \right\} \quad (17)$$

Equation (17) predicts a parabolic trend versus $\Delta V_{CNP}(c)$, whose curvature depends on the ratio between the mean charge carrier mobility $\langle \mu \rangle = \frac{\mu_h + \mu_e}{2}$ and the Fermi velocity $v_{F,rGO}$. In Figure 2f, we show that the best fit $\Delta I_{CNP}(c)$ versus $\Delta V_{CNP}(c)$ (dashed line) fulfills Equation (17). It is clear that $f(V_{CNP}) = -1$ for our data which makes the curvature concave. We also find a representative value for $V_{CNP,0}$ that yields $n_{NCP} = 1.32 \pm 0.62 \times 10^{12}$ cm^{-2}. The n_{CNP} value may be used to assess the variability of the rGO film. We highlight that the dependence on the concentration of the minimum current ΔI_{CNP} is embodied in its dependence on ΔV_{CNP}, hence their information content is strongly correlated.

5.3. The Electronic Properties of rGO Versus the Offset Gate Voltage V_{GS}–V_{CNP}

In **Figure 5**, we show the modulation of the electronic properties of rGO by the gate voltage V_{GS}–V_{CNP}. This representation is also practically viable, as it embodies the concentration dependence into the V_{CNP}, and hence it allows us to renormalize the curves into a single universal curve. This is clearly shown in Figure 5a where we plot the excess charge Δn versus V_{GS}–V_{CNP} at different concentrations. The trend reveals some weak but significant asymmetry around the V_{CNP}.

Figure 5b displays the sheet conductance plotted versus V_{GS}–V_{CNP}, which mimics the trend of the excess charge.

We then evaluate the dependence of charge carrier mobility on V_{GS}–V_{CNP} by means of Drude's theory (which may not be rigorous here for rGO,[41] as is a disordered material with restricted delocalization). We estimate the effective charge carrier mobility μ_{eff} from the well-known expression that links it to the sheet conductance $\sigma_{\blacksquare}$ and the charge carrier areal density n_{ch}:

$$\mu_{eff} = \frac{\sigma_{\blacksquare}}{e n_{ch}} = \left(\frac{L}{W} \frac{I_{DS}}{V_{DS}} \right) \frac{1}{e \left| n_{NCP} + \Delta n \left(V_{GS} - V_{CNP} \right) \right|} \quad (18)$$

The current is from Equation (15). The plot of Equation (17) in Figure 5c is calculated by neglecting n_{NCP} as it is often done in rGO papers by analogy with graphene. The plot exhibits the typical divergent cusp at the CNP. When n_{NCP} value estimated as in Section 5.2, is accounted for, the cusp at $V_{GS} = V_{CNP}$ is rounded up by the effects of the intrinsic dopants present in rGO and its maximum value (in this case close to 0.22 cm^2 V^{-1} s^{-1}) is attained (Figure 5d). These curves are skewed because of the asymmetry in the charge carrier mobilities already discussed.

To summarize, the protocol for data analysis consists of four steps:

i. Fit $\Delta V_{CNP}(c)$versus c data with Equation (10), to obtain K_a, $[P]_{G0}$, q and $(\mu_{0,PXG}+\mu_{0,PG})$ (Section 3.2);
ii. Fit the excess current $\Delta I_{DS}(c)$ versus c with Equation (15), to obtain μ_h, μ_e, $v_{f,rGO}$, $C_{DL,Ch}$, N_l (Section 5.1);
iii. Fit $\Delta I_{CNP}(c)$ versus c data with Equation (16), to obtain n_{hNCP} (Section 5.2);
iv. Calculate the relevant electronic properties versus c.

Our model is robust to operator-dependent data sorting. Above all, it is based on a physical-chemical model of immunorecognition and its coupling to the electronic structure of the active material rGO. Its value stems from the avoidance of a phenomenological ansatz to explain the relative variation of the current (signal) versus concentration. Instead, it yields the direct variation of the electronic properties of rGO in the EGT sensor that can be used to build a dose curve resting on the chemical–physical properties of the rGO-EGT sensor.

6. Conclusion

This work is the first attempt to explicitly introduce a physical-chemical description of an immunosensor based on the rGO electrolyte-gated transistor. Our effort is motivated by the importance of understanding at a more rigorous and less phenomenological level the key properties of an active material, here rGO, in transducing and possibly amplifying the biorecognition events that occur in the sensing device. The results and the concentration dependence of the electronic properties that we derive from an electrostatic model of the rGO-EGT and its application to our experimental data reveal that most of the effect is contained in the apparent shift of the charge neutrality point voltage V_{CNP}, and in a correlated manner into the minimum current of the rGO device I_{CNP}. The strong electrostatic coupling occurs because of the dominant quantum capacitance of the rGO (and not of the interfacial double-layer capacitance), which reflects the generation of extra charge carriers in the active material. The other parameters

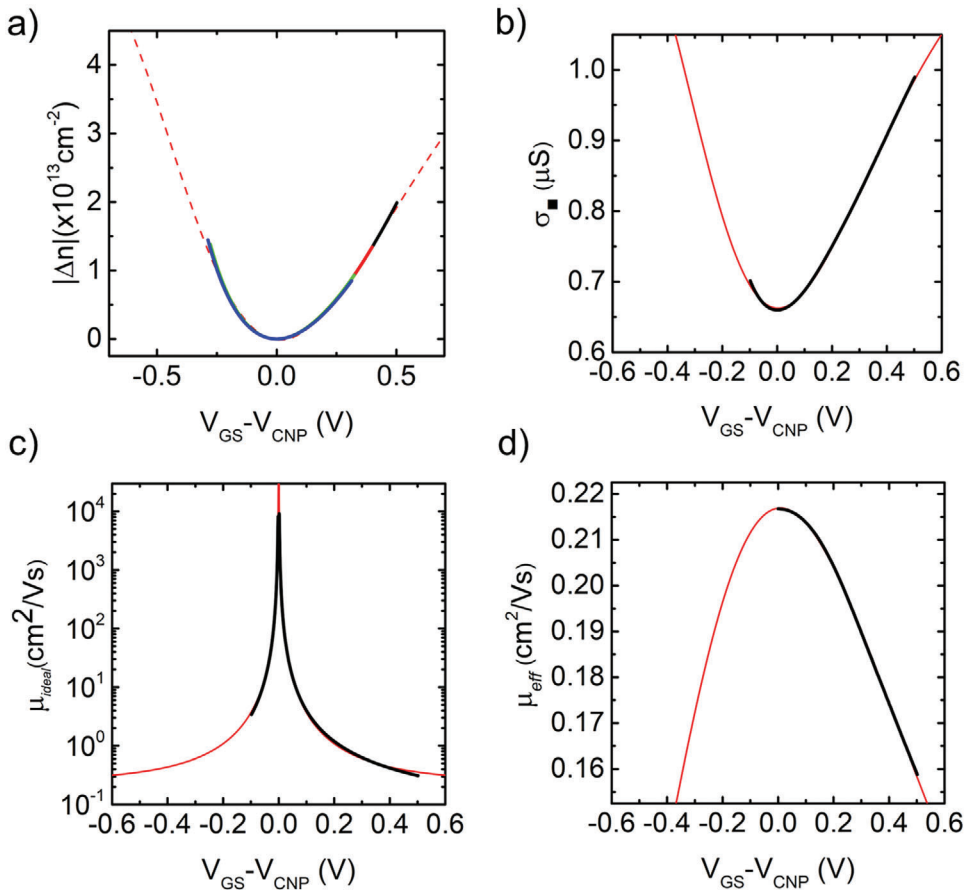

Figure 5. Electronic properties of rGO versus V_{GS}–V_{CNP}(c). a) Excess areal charge density Δn calculated from the best fit parameters and at four different analyte concentrations: 0 M, 1 fM, 1 pM, and 1 nM. The curves overlap perfectly as the result of the nearly-concentration independent interfacial capacitance C_{DL} and carrier areal density n_0 in Equation (14). The dashed lines show the trend according to Equation (14) in a range of voltages that were outside the present experiment; b) Sheet conductance of hole and electrons; c) Charge carrier mobility calculated with Equation (17) by neglecting the intrinsic n_{CNP} carrier density; d) Charge carrier mobility calculated with Equation (18) by accounting for the intrinsic charge carrier density.

that are routinely looked upon in sensing, like transconductance and charge carrier mobility are much less sensitive to the concentration and apparently useless for quantifying the concentration of the target analyte.

From a fundamental point of view is important to understand how the biorecognition events in the rGO-EGT immunosensor couple to the electronic properties of the rGO-EGT also for guiding the optimization of a device, maximizing the information contained in the multiparametric response. Another more specific goal is to avoid a priori choices of isotherm curves for describing the sensor response, which we show may be misleading in the interpretation, besides the capability to invert the signal of the dose curve to yield the concentration. We believe that this work provides a framework for a rigorous analysis of the biosensor response, with no a priori choices and data discrimination, instead using the whole information contained in the experimental data.

The approach that we devised starts from the thermodynamic equilibrium of biorecognition between a gate electrode functionalized with specific recognition probes and the solution of interest containing the target analyte species. We considered a single equilibrium of binding, but it can obviously be modified for more complicated equilibria or competing reactions. Then, the target-equilibrated gate electrode is placed in the electrolyte gating the rGO-transistor, so a new equilibrium is attained. Our simple model shows that robust electrodes (hence measurements) require to keep most of the bound target analyte on the gate electrode, so the binding constant between target and probe K_a must be high, and the activity of the probe at the electrode should be also large. This is the first sound result that provides a guideline to assess the processing of the functionalized electrodes. However, we note that the outcome is a direct consequence of the choice of a single equilibrium in the recognition between probe and target, and different reaction schemes at equilibrium, or an effective nonequilibrium condition in the two-step incubation/measurement may change this guideline. Breeching these intuitive conditions may lead to poorly specific and ineffective sensors, even for an excellent performance of the transducer.

Then, we have modeled the concentration-dependent potential profile across the gate/electrolyte/rGO, to derive the analytical equations (and some simplified forms in limited useful cases) that describe the modulation of the areal charge density in rGO. The value of our model is that the active material enters

explicitly into the picture through the distinctive quantum capacitance of the 2D material and the large interfacial capacitance. Albeit we accept that objections to an oversimplification of a not easy-to-control material could be made, the model introduces structural elements and assessed properties of the rGO together with the functionalized gate on the same footings, with well-defined hypotheses and literature support. The outcome is that we analytically derive the concentration dependence of both the CNP and the excess charge density governed by the gate voltage and the concentration of the target analyte (that modulates the potential of the gate voltage). We are then able to cast the explicit expressions of the current at the CNP and the current at any gate voltage. We prove that our global fitting on the whole data set acquired with different gate voltages, different devices, and numerous different analyte concentrations, can be accurately fitted using a small set of fitting parameters for the CNP voltage that allow us to extract the binding constant and the probe activity/concentration on the electrode. Then, from the trend of the minimum device current, keeping the previous parameters fixed, we extract the product of the mean charge mobility and the charge carrier density n_0, which we show depends on the functionalization at the gate and the concentration. Finally, by only three parameters, viz. the charge carrier mobilities of electrons and holes, and the interfacial capacitance of rGO (the latter linked to n_0) we nicely reproduce the whole transfer curves of the rGO-EGT. The fit is not only accurate, but also consistent with the observation that was made by us with a heuristic approach in a recent paper[19] that the curvature and the transconductances of holes and electrons are not sensitive to concentration. Our model explains why this happens with physical arguments with no a priori condition. The model also clearly shows that the response of the rGO-EGT biosensors is largely dominated by the concentration-dependent shift of the V_{CNP}, while the effective areal capacitance and the related charge density are less sensitive to concentration, hence to recognition.

Significantly, this is the first time that an experimental dose curve is reproduced by a materials theory of the electronic biosensor, which is important for understanding the physical origin of the response of biosensors, beyond the usual phenomenological approach.[13] This, per se, is already an original contribution, as the materials aspects in biosensing are often disguised, or "hidden under the carpet", provided the (bio)sensor works effectively. We point out that for biosensors based on conductive or semiconductive thin films, such as conjugated polymers or molecules, carbon nanotubes, MXenes or metal oxides, and graphene-related materials the electronic structure theory must be tailored to the characteristics of the active material, in way similar to what we did here for rGO. For this, the synergy with multiscale modeling of materials for sensing is crucial.

We are convinced that this change of perspective is important and timely since the knowledge produced by approaches like the one shown here is fundamental to driving the technology toward a rational design of devices, processes, and measurements. This will be a change of paradigm that will enable reliable diagnostics, monitoring of environmental parameters, and sensing in personalized medicine.

7. Experimental Section

For the expansion of the equations, Wolfram Alpha was used. The experimental data used for the analysis in this manuscript were published in Ref. [19]

Acknowledgements

This work was funded by the ERA-NET EuroNanoMedIII project AMI. The publication has been realized with the co-financing of European Union – FSE-REACT-EU, PON research and Innovation 2014–2020 DM1062/2021. The authors acknowledge the project EC PRIMA – FRUALGAE. This Project has received funding from the European Union's Horizon 2020 research and innovation program under the Marie Sklodowska–Curie Grant Agreement 872217. Activity in Strasbourg was also supported by the EC through the ERC project SUPRA2DMAT (GA-833707) and the HORIZON-CL4-2023-DIGITAL-EMERGING-01-CNECT project 2D-PRINTABLE (GA-101135196). R.F.O. acknowledges further support from the Sao Paulo Research Foundation FAPESP (2021/06238-5) and INCT/INEO (Brazil). The research leading to these results has received funding from the European Union – NextGenerationEU through the Italian Ministry of University and Research under PNRR – M4C2-I1.3 Project PE_00000019 "HEAL ITALIA" to Carlo Augusto Bortolotti and Marcello Berto, CUP E93C22001860006. The views and opinions expressed are those of the authors only and do not necessarily reflect those of the European Union or the European Commission. Neither the European Union nor the European Commission can be held responsible for them. This work had received funding from the European Union's Horizon Europe research and Innovation program under grant agreement No.101098597, project Piezo4Spine (F.B and P.G).

Conflict of Interest

The authors declare no conflict of interest.

Data Availability Statement

The data that support the findings of this study are openly available in [Zenodo] at [https://doi.org/10.5281/zenodo.8138121], reference number [8138121].

Keywords

ambipolar transistor, bioelectronics, immunosensor, reduced graphene oxide

Received: November 6, 2023
Revised: December 22, 2023
Published online: January 14, 2024

[1] F. Torricelli, D. Z. Adrahtas, Z. Bao, M. Berggren, F. Biscarini, A. Bonfiglio, C. A. Bortolotti, C. D. Frisbie, E. Macchia, G. G. Malliaras, I. Mcculloch, M. Moser, T.-Q. Nguyen, R. M. Owens, A. Salleo, A. Spanu, L. Torsi, *Nat. Rev. Methods Prim.* **2021**, *1*, 66.

[2] M. Berto, M. Di Giosia, M. Giordani, M. Sensi, F. Valle, A. Alessandrini, C. Menozzi, A. Cantelli, G. C. Gazzadi, F. Zerbetto, M. Calvaresi, F. Biscarini, C. A. Bortolotti, *Adv. Electron. Mater.* **2021**, *7*, 200114.

[3] S. P. White, K. D. Dorfman, C. D. Frisbie, *J. Phys. Chem. C* **2016**, *120*, 108.
[4] R. Hasler, C. Reiner-Rozman, S. Fossati, P. Aspermair, J. Dostalek, S. Lee, M. Ibanez, J. Bintinger, W. Knoll, *ACS Sens.* **2022**, *7*, 504.
[5] K. Guo, S. Wustoni, A. Koklu, E. Díaz-Galicia, M. Moser, A. Hama, A. A. Alqahtani, A. N. Ahmad, F. S. Alhamlan, M. Shuaib, A. Pain, I. Mcculloch, S. T. Arold, R. Grünberg, S. Inal, *Nat. Biomed. Eng.* **2021**, *5*, 666.
[6] M. Sensi, G. Migatti, V. Beni, T. M. D'alvise, T. Weil, M. Berto, P. Greco, C. Imbriano, F. Biscarini, C. A. Bortolotti, *Macromol. Mater. Eng.* **2022**, *307*, 2100880.
[7] E. Macchia, K. Manoli, B. Holzer, C. Di Franco, M. Ghittorelli, F. Torricelli, D. Alberga, G. F. Mangiatordi, G. Palazzo, G. Scamarcio, L. Torsi, *Nat. Commun.* **2018**, *9*, 3223.
[8] M. Sensi, M. Berto, S. Gentile, M. Pinti, A. Conti, G. Pellacani, C. Salvarani, A. Cossarizza, C. A. Bortolotti, F. Biscarini, *Chem. Commun.* **2021**, *57*, 367.
[9] P. A. Manco Urbina, M. Berto, P. Greco, M. Sensi, S. Borghi, M. Borsari, C. A. Bortolotti, F. Biscarini, *J. Mater. Chem. C* **2021**, *9*, 10965.
[10] K. Solodka, M. Berto, D. Ferraro, C. Menozzi, M. Borsari, C. A. Bortolotti, F. Biscarini, M. Pinti, *Adv. Mater. Interfaces* **2022**, *9*, 2102341.
[11] H. Swenson, N. P. Stadie, *Langmuir* **2019**, *35*, 5409.
[12] A. Paradisi, M. Berto, M. Di Giosia, S. Mazzali, M. Borsari, T. D. Marforio, F. Zerbetto, M. Calvaresi, A. Orieshyna, N. Amdursky, C. A. Bortolotti, F. Biscarini, *Chem.–A Eur. J.* **2023**, *29*, 202301704.
[13] M. Berto, S. Casalini, M. Di Lauro, S. L. Marasso, M. Cocuzza, D. Perrone, M. Pinti, A. Cossarizza, C. F. Pirri, D. T. Simon, M. Berggren, F. Zerbetto, C. A. Bortolotti, F. Biscarini, *Anal. Chem.* **2016**, *88*, 12330.
[14] M. Galliani, C. Diacci, M. Berto, M. Sensi, V. Beni, M. Berggren, M. Borsari, D. T. Simon, F. Biscarini, C. A. Bortolotti, *Adv. Mater. Interfaces* **2020**, *7*, 2001218.
[15] C. Reiner-Rozman, C. Kotlowski, W. Knoll, *Biosensors* **2016**, *6*, 17.
[16] C. Diacci, J. W. Lee, P. Janson, G. Dufil, G. Méhes, M. Berggren, D. T. Simon, E. Stavrinidou, *Adv. Mater. Technol.* **2020**, *5*, 00262.
[17] M. Giordani, M. Sensi, M. Berto, M. Di Lauro, C. A. Bortolotti, H. L. Gomes, M. Zoli, F. Zerbetto, L. Fadiga, F. Biscarini, *Adv. Funct. Mater.* **2020**, *30*, 2070187.
[18] V. Parkula, M. Berto, C. Diacci, B. Patrahau, M. Di Lauro, A. Kovtun, A. Liscio, M. Sensi, P. Samorì, P. Greco, C. A. Bortolotti, F. Biscarini, *Anal. Chem.* **2020**, *92*, 9330.
[19] M. Sensi, R. F. De Oliveira, M. Berto, M. Palmieri, E. Ruini, P. A. Livio, A. Conti, M. Pinti, C. Salvarani, A. Cossarizza, J. M. Cabot, J. Ricart, S. Casalini, M. B. González-García, P. Fanjul-Bolado, C. A. Bortolotti, P. Samorì, F. Biscarini, *Adv. Mater.* **2023**, *35*, 2211352.
[20] S. Dröscher, P. Roulleau, F. Molitor, P. Studerus, C. Stampfer, K. Ensslin, T. Ihn, *Appl. Phys. Lett.* **2010**, *96*, 152104.
[21] F. Parhizgar, A. Qaiumzadeh, R. Asgari, *Phys. Rev. B* **2017**, *96*, 075447.
[22] S. Vasilijevic, G. Mattana, G. Anquetin, N. Battaglini, B. Piro, *Electrochim. Acta* **2021**, *371*, 137819.
[23] S. Vasilijevic, R. Boukraa, N. Battaglini, B. Piro, *Synth. Met.* **2023**, *295*, 117355.
[24] X. Du, H. Guo, Y. Jin, Q. Jin, J. Zhao, *Electroanalysis* **2015**, *27*, 2760.
[25] F. Chen, Q. Qing, J. Xia, J. Li, N. Tao, *J. Am. Chem. Soc.* **2009**, *131*, 9908.
[26] A. Das, S. Pisana, B. Chakraborty, S. Piscanec, S. K. Saha, U. V. Waghmare, K. S. Novoselov, H. R. Krishnamurthy, A. K. Geim, A. C. Ferrari, A. K. Sood, *Nat. Nanotechnol.* **2008**, *3*, 210.
[27] Y. Sabir, S. M. Chaudhry, *Proc. Natl. Acad. Sci. India Sect. A – Phys. Sci.* **2018**, *88*, 317.
[28] J. Xia, F. Chen, J. Li, N. Tao, *Nat. Nanotechnol.* **2009**, *4*, 505.
[29] F. Su, L. Huo, Q. Kong, L. Xie, C. Chen, *Catalysts* **2018**, *8*, 444.
[30] H. Xu, Z. Zhang, L.-M. Peng, *Appl. Phys. Lett.* **2011**, *98*, 133122.
[31] H. K. F. Abadi, R. Yusof, S. D. Naghib, M. T. Ahmadi, M. Rahmani, M. J. Kiani, M. Ghadiri, *J. Comput. Theor. Nanosci.* **2014**, *11*, 596.
[32] F. Lima, G. Maia, *RSC Adv.* **2014**, *4*, 22575.
[33] M. Beeg, A. Nobili, B. Orsini, F. Rogai, D. Gilardi, G. Fiorino, S. Danese, M. Salmona, S. Garattini, M. Gobbi, *Sci. Rep.* **2019**, *9*, 2064.
[34] S. Liang, J. Dai, S. Hou, L. Su, D. Zhang, H. Guo, S. Hu, H. Wang, Z. Rao, Y. Guo, Z. Lou, *J. Biol. Chem.* **2013**, *288*, 13799.
[35] F. S. Damos, R. C. S. Luz, L. T. Kubota, *Langmuir* **2005**, *21*, 602.
[36] L. Li, C. Li, Z. Zhang, E. Alexov, *J. Chem. Theory Comput.* **2013**, *9*, 2126.
[37] R. Furlan De Oliveira, V. Montes-García, P. A. Livio, M. B. González-García, P. Fanjul-Bolado, S. Casalini, P. Samorì, *Small* **2022**, *18*, 2201861.
[38] R. Furlan De Oliveira, P. A. Livio, V. Montes-García, S. Ippolito, M. Eredia, P. Fanjul-Bolado, M. B. González García, S. Casalini, P. Samorì, *Adv. Funct. Mater.* **2019**, *29*, 1905375.
[39] N. Lago, M. Buonomo, R. C. Hensel, F. Sedona, M. Sambi, S. Casalini, A. Cester, *IEEE Trans. Electron Devices* **2022**, *69*, 3192.
[40] J. R. F. Lima, *Phys. Lett. Sect. A Gen. At. Solid State Phys.* **2015**, *379*, 179.
[41] A. Kovtun, A. Candini, A. Vianelli, A. Boschi, S. Dell'elce, M. Gobbi, K. H. Kim, S. Lara Avila, P. Samorì, M. Affronte, A. Liscio, V. Palermo, *ACS Nano* **2021**, *15*, 2654.